Effects of axial static stress and confining pressure on the dynamic compressive behaviours of granite

Shaosen Ma, Weizhong Chen & Wusheng Zhao

Published online: 28 Jan 2019.

Submit your article to this journal ⬚

Article views: 10

View Crossmark data ⬚

Taylor & Francis
Taylor & Francis Group

Check for updates

Effects of axial static stress and confining pressure on the dynamic compressive behaviours of granite

Shaosen Ma[a], Weizhong Chen[a,b] and Wusheng Zhao[b]

[a]Research Centre of Geotechnical and Structural Engineering, Shandong University, Jinan, China; [b]State Key Laboratory of Geomechanics and Geotechnical Engineering, Institute of Rock and Soil Mechanics, Chinese Academy of Sciences, Wuhan, China

ABSTRACT

This study aims to investigate experimentally the effects of axial static stress and confining pressure on the dynamic compressive behaviours of granite. A new index of confining pressure increase factor (CPIF) was introduced to evaluate the confining pressure-induced strength enhancement, a modified definition was proposed to determine the dynamic deformation modulus, and the roles of energy storage limit (ESL) were highlighted to explain the energy absorption and release process. The results showed that when the axial static stress was less than a threshold value that was equivalent to the rock's elastic limit, it coupled with the confining pressure and elicited positive effects on the strength enhancement of the rock. However, once the threshold value was exceeded, the axial static stress weakened the rock while the confining pressure began to strengthen the rock in a more significant way. Moreover, the dynamic deformation modulus increased as the static stresses increased (including axial static stress and confining pressure) when the rock remained in the linear elasticity under the static loading, while it declined when the rock suffered from damage before the impact. Furthermore, the results revealed that the ESL tended to play critical roles in the process of energy absorption and release in different situations.

1. Introduction

In mining engineering, during tunnel or cavern construction, resource exploitation and other underground excavations at great depths, the rock masses are often subjected to high-static and dynamic loads simultaneously, commonly referred to as coupled static–dynamic loads (Zhou, Li, Zou, Jiang, & Li, 2014). Specifically, the static loads may originate from the gravity stress or tectonic stress, and the dynamic loads may arise from the drilling, blasting or earthquakes. The behaviours of rock subjected to such coupled loads are completely different to those elicited when the same rock mass is subjected separately to either static or dynamic loads (Li et al., 2016; Zhang, Mishra, & Heasley, 2015).

During the development of the various laboratory techniques that can provide the coupled static–dynamic loading (Xia & Yao, 2015; Zhang & Zhao, 2014), many experimental investigations

---

have been conducted to explore the dynamic behaviours of rocks based on 1D or 3D static pre-stresses. Most of these investigations focussed on the following four aspects:

1. Dynamic compressive behaviours of rocks at increased strain rates: various experimental studies have been conducted to investigate the compressive behaviours of rocks under the dynamic loading on a split Hopkinson pressure bar (SHPB) system. The results showed that the stress–strain curves of rocks following an impact differed from those subjected to static compression in terms of the peak stress, total strain, etc. (Mohr, Gary, & Lundberg, 2010). Subsequently, a consensus was reached based on which the rock was considered as strain-rate-dependent and its compressive strength increased as a function of the strain rate (Hashiba & Fukui, 2015; Liang, Zhang, Li, & Xin, 2016). Yet, not all investigators agreed in regard to the strain rate at which such an increase would become significant (Mishra, Meena, Chakraborty, Chandel, & Singh, 2017). Furthermore, it was suggested that the deformation modulus grew as a function of the strain rate, while some deviations were documented in the pre-peak and post-peak strain characteristics (Munoz, Taheri, & Chanda, 2016; Sun, Li, Yang, Fan, & Sun, 2016). Additionally, the positive relationship between the energy absorption ratio and the compressive strength or strain rate were discussed (Feng et al., 2016; Wang, Xu, Fang, & Wang, 2017). Moreover, the failure patterns were observed and classified into different types, such as the apparently intact, single fracturing or split, and multiple fracturing or pulverisation types.

2. Dynamic compressive behaviours of rocks under the axial static stress, confining pressure or 3D static stresses: many uni-axial and tri-axial dynamic compression tests were conducted, and the results showed that the rock's strength was sensitive to the confining pressure at a particular strain rate, and increased as a function of the increasing confining pressure (Li, Tao, Wu, Du, & Wu, 2017; Saksala, 2016). Additionally, the rock under a certain confining pressure elicited strain rate dependence, which was approximately similar to that observed in routine impact tests (Saksala, Hokka, & Kuokkala, 2017). Correspondingly, some tests were devised and executed to investigate the variation laws of the dynamic stress–strain curve, compressive strength, deformation modulus and dissipation energy of rocks under the different combined static stresses (Liu & He, 2012; Liu, Li, & Chen, 2017). Furthermore, the failure patterns of rocks under the coupled loads were also different, which can be divided into three groups, namely the shear, cataclasis and cleavage (Niu, Li, Liu, Li, & Peng, 2015). Moreover, some optional measurement methods, including the X-ray micro CT, laser measurement, digital image correlation, and the caustics technique, were employed to monitor the small deformations or fragmentation (Zhang & Zhao, 2014).

3. Dynamic tensile behaviours of rocks: the Brazilian disc (BD) tests were gradually extended to the dynamic tests. In particular, Zhao and Li (2000) investigated the dynamic tensile behaviours of granite with BD specimens. Wang, Li, and Song (2006) undertook dynamic tests on a SHPB system with flattened BD specimens. Subsequent to these, many scholars studied further the dynamic tensile behaviours of rocks, including the tensile strength, strain rate dependence and failure patterns (Wang & Shi, 2017), in which the axial static pre-stress was also taken into consideration (Wu, Chen, & Xia, 2015).

4. Other experimental works: some innovative tests were performed to examine the dynamic mechanical properties of rocks at various temperatures or in different saturation conditions (Zhao, Liu, Jiang, Wang, & Huang, 2016).

In regard to the dynamic compressive behaviours of granite based on the 3D coupled static–dynamic loading, even though the aforementioned achievements have been accomplished, some disadvantages still remain, such as the fact that (a) the strength attenuation of rocks caused by increased axial static stress was not investigated in depth, (b) the existing index does not evaluate accurately the strength enhancement of rocks corresponding to increasing

confining pressures, (c) a uniform definition of the dynamic deformation modulus was not properly considered and (d) the roles of the energy storage limit (ESL) in the transformation mechanism of energy absorption and release were not discussed in detail. It is worth noting that all of these are improved to some extent in this study.

This study aims to investigate experimentally the effects of axial static stress and confining pressure on the dynamic mechanical properties and behaviours of granite under the 3D coupled static–dynamic loading, in terms of the stress–strain curve, failure pattern, compressive strength, deformation modulus and energy absorption and release process. Simultaneously, it introduces a new index to evaluate the confining pressure-induced strength enhancement, and highlights the roles of ESL to demonstrate the energy transformation during the impact. Furthermore, it outlines some favourable conclusions and experimental results for the establishment of the rock burst criterion used in deep underground engineering in future studies.

2. Test details

2.1. Preparatory works

The granite was drilled from an underground energy storage site in Gansu, China, at depths within the range of 350–400 m. Special care was taken to manufacture the cylindrical specimen with a diameter of 50 mm and a length of 30 mm. Each of these specimens were then polished to have a surface roughness that was <0.02 mm and an end-surface that was perpendicular to the axis with a tolerance that was <0.001 rad (Tian, Chen, Yang, & Yang, 2015), as shown in Figure 1.

The physical properties of the specimens were studied. The average density was 2579 kg/m^3, and the average P-wave velocity was 4065 m/s. The chemical compositions of the specimens were then investigated, and their average proportions are presented in Table 1.

A series of uni-axial and tri-axial static compression tests were conducted on a RMT-150C servo-controlled testing machine at the strain rate of 10^{-5} s^{-1} (pseudo-static) (ASTM, 2001), and the results are listed in Table 2. Based on the stress–strain curves, the elastic limit was treated as the point where the curve began to deviate from the initial straight line and at which the slope started to decrease, which suggested that plastic deformation and internal damage within the rock started to occur. In addition, the elastic limit considered in this section is the same as the limits encountered in subsequent sections.
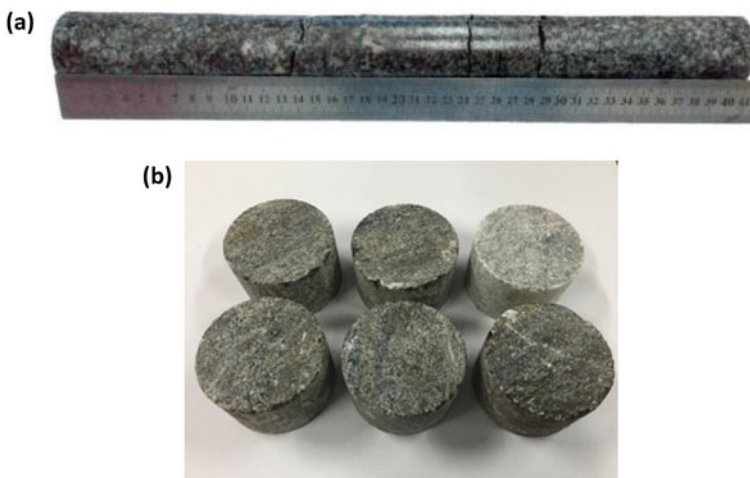

Figure 1. Images of the granite specimens: (a) one of the geological boreholes of granite; (b) part of the standard specimens.

Table 1. Chemical compositions of the specimens (%).

SiO_2	Al_2O_3	CaO	MgO	Fe_2O_3	FeO	MnO	TiO_2	K_2O	Na_2O	Soluble residue
71.88	14.34	1.43	1.14	0.88	1.55	0.05	0.31	4.13	4.11	0.18

Table 2. Static mechanical parameters of the specimens (MPa).

	Confining pressure (MPa)			
	0	5	10	15
Static compressive strength (MPa)	110.01	132.05	161.27	182.06
Elastic limit (MPa)	76.36	89.63	107.21	127.30
Deformation modulus (GPa)	30.65	30.94	31.19	31.72

Some routine impact tests (without axial static stress and confining pressure) were performed on the SHPB system at an approximate strain rate of $90\,s^{-1}$ (Zhou et al., 2012), the average dynamic compressive strength was 162.42 MPa, and the average deformation modulus was 38.46 GPa.

2.2. Test system and procedure

The dynamic compression tests were conducted using a modified SHPB system, as shown in Figure 2(a).

The SHPB system consists of a gas tank, a pressure vessel, a shuttle-shaped striker, an incident bar, a transmission bar, a momentum bar and axial static stress and confining pressure components. The shuttle-shaped striker can produce good repeatability of half-sine pulse waves to reduce the high frequency oscillations and minimise the dispersion effect (Li, Lok, Zhao, & Zhao, 2000). The striker and bars were made from the high strength 40Cr steel with nominal yield strength of 800 MPa. Two sets of strain gauges were respectively attached on the incident bar and transmission bar, and each of them consisted of two gauges (2×2 mm) located diametrically opposite to each other. The axial static stress can be applied by an axial static stress component (that ranged from 0 to 200 MPa). The confining pressure can be loaded based on a confining pressure component (that ranged from 0 to 100 MPa). The dynamic loading can be provided by the striker whose velocity was controlled by the air pressure in the gas vessel. The experimental data can be collected and processed by the super-dynamic strain meter, computer and digital oscilloscope, which are not shown in the schematic of the equipment in Figure 2(a).

During the test, the mechanical states of the specimen can be divided into two stages, as follows.

At the first stage, before impacting, the axial static stress and confining pressure were applied on the specimen, and the static stress equilibrium occurred in the axial direction (stress equilibrium was also achieved in the circumferential direction owing to σ_c), as shown in Figure 2(b).

Herein, the forces P_{01} and P_{02} on both ends of the specimen can be formulated as follows:

$$P_{01} = P_{02} = \sigma_0 A_b \tag{1}$$

where, A_b is the cross-sectional area of the bars; σ_0 is the axial static stress.

At the second stage, after impacting, a compressive wave propagated in the incident bar as an incident wave owing to the impact of the striker on the free-end of the incident bar. The incident wave then reached the incident bar-specimen interface, and part of the wave was reflected back (reflected wave), and the remainder passed through the specimen and entered the transmission bar as a transmitted wave (Zhou et al., 2014), as illustrated in Figure 2(c). The incident, reflected and transmitted waves can be calculated individually using the strains ε_i, ε_r, ε_t, which were derived from the corresponding strain gauges.
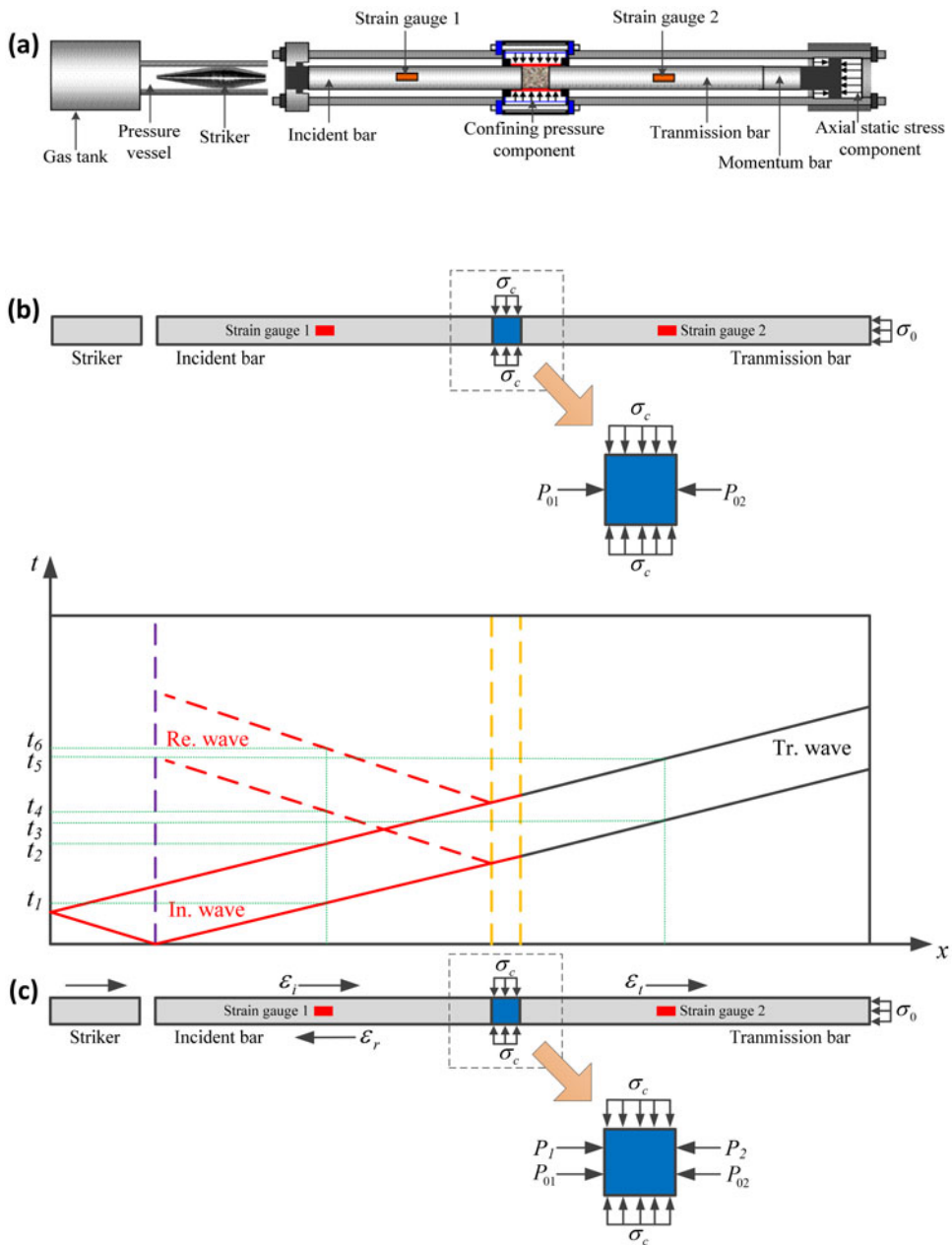
Figure 2. Modified SHPB system: (a) equipment schematic; (b) mechanical state of the specimen before impacting; (c) wave propagation and mechanical state of the specimen after impacting.

Herein, the forces P_1 and P_2 on both ends of the specimen can be calculated as follows (Latham, Van Meulen, & Dupray, 2006):

$$P_1(t) = EA_b[\varepsilon_i(t) + \varepsilon_r(t)] \tag{2}$$

$$P_2(t) = EA_b\varepsilon_t(t) \tag{3}$$

where, E is the elastic modulus of the bars.

Several micro-seconds later, the dynamic stress equilibrium occurred in the axial direction, as follows:

$$P_{01} + P_1 = P_{02} + P_2 \tag{4}$$

Furthermore, the histories of stress $\sigma(t)$ and strain $\varepsilon(t)$ of the specimen can be taken by the following equations (Dai, Huang, Xia, & Tan, 2010):

$$\sigma(t) = E\varepsilon_t(t) \tag{5}$$

$$\varepsilon(t) = -\frac{2C}{L}\int_0^t \varepsilon_r(t)dt \tag{6}$$

where, C is the wave velocity in the bars; L is the length of the specimen.

Moreover, the incident energy E_I, reflected energy E_R, and transmitted energy E_T can be indicated as follows:

$$\begin{cases} E_I = EA_bC\int_0^T \varepsilon_i^2(t)dt \\ E_R = EA_bC\int_0^T \varepsilon_r^2(t)dt \\ E_T = EA_bC\int_0^T \varepsilon_t^2(t)dt \end{cases} \tag{7}$$

Regardless of the kinetic energy, thermal energy, etc., the absorbed energy of the specimen E_S can be calculated as follows:

$$E_S = E_I - E_R - E_T = EA_bC\left[\int_0^T \varepsilon_i^2(t)dt - \int_0^T \varepsilon_r^2(t)dt - \int_0^T \varepsilon_t^2(t)dt\right] \tag{8}$$

Due to that:

$$A_s = A_b \tag{9}$$

where, A_s is the cross-sectional area of the specimen.

The absorbed energy per unit volume U_S can then be obtained from the following equation:

$$U_S = \frac{E_S}{V_S} = \frac{EC}{L}\left[\int_0^T \varepsilon_i^2(t)dt - \int_0^T \varepsilon_r^2(t)dt - \int_0^T \varepsilon_t^2(t)dt\right] \tag{10}$$

2.3. Test scheme

Sixteen cases were set up. Specifically, four typical levels of axial static stresses (25, 50, 75 and 100 MPa) and four typical levels of confining pressures (0, 5, 10 and 15 MPa) were chosen, and the strain rates were controlled at a value that equalled $\sim 90\,s^{-1}$. It is worth demonstrating the source of the given static stresses, whereby the four levels of confining pressures were derived from experimental cases as previously reported in publications by numerous scholars, including Professors Xibing Li and Fengqiang Gong. Both scholars had clearly demonstrated the validation of these confining pressures that were used for deep-rock masses (Gong et al., 2011; Li et al., 2009). The four levels of axial static stresses were carefully designed by the authors, and were based on the results of the uni-axial and tri-axial static compression tests. The rock specimens tended to enter different stages under the given axial static stresses before impacting, such as the linear elasticity, early damage, late damage or even the yield stage. And it was more effective and helpful to investigate the effects of the axial static stress with such different case settings. In addition, there were several duplicate tests for each case, and three similar results were used for the follow-up discussions.

3. Test results and discussions

3.1. Dynamic stress–strain curve features

Sixteen typical dynamic stress–strain curves were chosen and shown in Figure 3.

At the beginning of the curve, there is a linear relationship between stress and strain in accordance to Hooke's law that is indicative of a linear elastic response. As the stress increases, the curves deviate from the initial straight line responses and exhibit nonlinear dependencies, thus showing that the rocks begin to produce internal damage and plastic deformation, and simultaneously tend to yield. After the peak, the curves shift downward and the stress begins to drop, thus suggesting that serious damages or macroscopic slips along some certain fracture surfaces occur.

Compared with the static cases (Jiang, Zhong, Cui, Feng, & Song, 2016), there are three special features associated with the dynamic stress–strain curves. Firstly, no concave segment appears at the beginning, that is, no typical compaction stage emerges, which is attributed to the fact that the initial compaction deformation of the rock has already been completed before the impact. Secondly, no straight line response emerges before the peak, but instead, a special 'two-segment' line occurs, with each line segment possessing a constant slope. Thirdly, a 'strain rebound' phenomenon occurs at the end, thus showing that the total strain decreases during the unloading process, which is owing to the elastic strain recovery when the internal elastic force within the rock exceeds the external loading force. Moreover, under different combined static stresses, the curves also exhibit different trends in terms of the peak stress, pre-peak slope and post-peak strain.
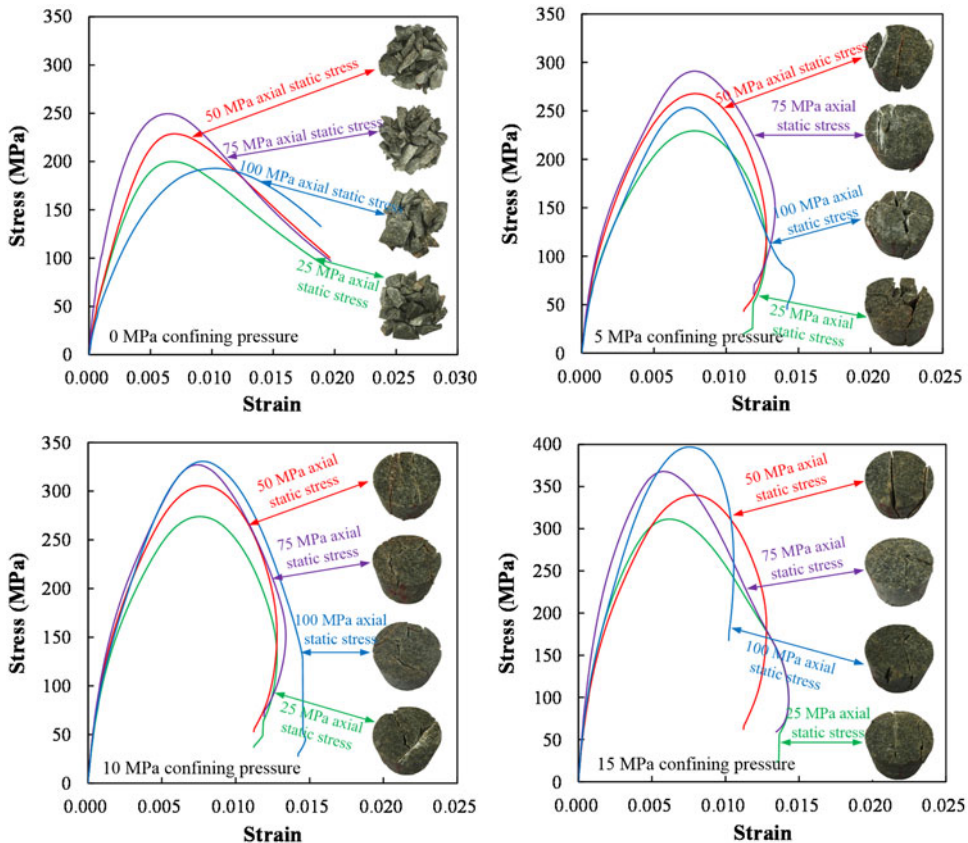

Figure 3. Typical dynamic stress–strain curves.

In addition, the schematics of the specimens after impacting were represented alongside the curves, as shown in Figure 3. The rock specimens failed with the compression–shear patterns (Xia & Yao, 2015). In particular, the failure patterns were further classified into two groups: the first is the group where the rock was only spalled outside the compression–shear surfaces. In this situation, the overall structural stability was maintained. The second is the group where the rock was spalled outside the compression–shear surfaces and simultaneously crushed inside the surfaces. In this circumstance, the rock appeared to exhibit an overall instability. Additionally, the rock's destructiveness dropped when the confining pressure increased, and enhanced when the axial static stress increased (Du, Dai, Xu, Liu, & Xu, 2018).

3.2. Dynamic compressive strength characteristics

The dynamic compressive strengths of rocks are presented in Table 3, and their variation laws with the axial static stress or confining pressure are illustrated in Figure 4.

From Figure 4(a), it can be observed that there is a growth in the compressive strength in the domain of low-axial static stresses. Subject to the continuous growth of the axial static stress, the strength may decrease, especially under low-confining pressures. This shows that the axial static stress tends to play opposite roles in the strength enhancement of rocks in different situations. Li, Lok, and Zhao (2005) revealed that micro-cracks exist within the rock initially, and their surfaces can reflect the dynamic compression waves and can transform them into tensile waves. Moreover, the reflected tensile waves can accelerate the crack generation, propagation, nucleation and aggregation, which would reduce the overall bearing capacity of the rocks.

Regarding the variations in Figure 4(a), when the confining pressures are high (10 or 15 MPa), the axial static stresses (25, 50, 75 and 100 MPa) are less than the elastic limits (107.21 or 127.30 MPa), and the rock remains in the elastic stage before the impact. The axial static stress is involved in the suppression of the micro-crack propagation, results in crack closure and makes the dynamic stress waves travel without too much reflection and transformation during the impact, thus preventing rock failure and leading to the improvement of its strength (Li et al., 2009). Conversely, under low-confining pressures (0 or 5 MPa), when the axial static stress increases to the value (100 MPa) larger than the elastic limits (76.36 or 89.63 MPa) and the rock enters the damage stage under the static loading. The axial static stress is involved in promoting the generation of micro-cracks, and involved in inducing increased reflection on the newly formed surfaces and increased transformation into dynamic tensile waves under the coupled

Table 3. Dynamic compressive strengths of rocks.

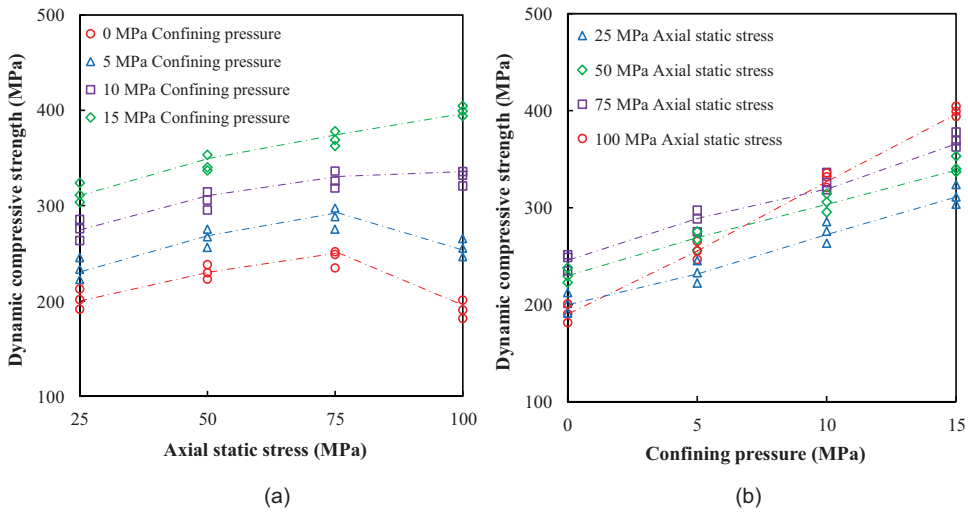|			Dynamic compressive strength (MPa)		
No.	Axial static stress (MPa)	Confining pressure (MPa)	Test 1	Test 2	Test 3
1	25	0	212.56	191.43	201.41
2	50	0	229.63	238.14	222.97
3	75	0	234.69	251.61	248.78
4	100	0	190.59	181.60	200.96
5	25	5	222.49	233.13	245.42
6	50	5	256.07	267.34	275.42
7	75	5	275.34	297.46	288.51
8	100	5	265.48	246.52	255.43
9	25	10	275.81	263.42	285.63
10	50	10	295.43	305.81	314.42
11	75	10	336.30	318.46	325.83
12	100	10	320.74	331.81	335.88
13	25	15	303.63	311.14	323.91
14	50	15	340.11	336.92	353.25
15	75	15	377.98	362.66	368.99
16	100	15	404.61	399.31	394.17

Figure 4. Variation laws of dynamic compressive strength (a) with axial static stress; (b) with confining pressure.

loading, thereby ultimately lowering the rock strength. The transformation role of the axial static stress in the strength enhancement takes place at a particular threshold value, which is equivalent to the rock's elastic limit.

In Figure 4(b), it is observed that the compressive strength of the rock increases as a function of the increasing confining pressure under the coupled loading. The confining pressure tends to suppress the micro-crack propagation and strengthen the rock, which can be demonstrated by the aforementioned mechanism (the increased confining pressure that can make the rock produce the internal damage was not taken into consideration because this was unusual in engineering projects). Moreover, it is worth noting that the confining pressure has a positive effect on the strength enhancement of rock, but the extent varies. In order to study this positive and variable effect, a new index of confining pressure increase factor (CPIF) was introduced to evaluate the confining pressure-induced strength enhancement, and it is defined as follows:

$$\text{CPIF} = \frac{f_c}{f_0} \tag{11}$$

where, f_c and f_0 are the compressive strengths of rock under a particular level of confining pressure and under no confining pressure, respectively. It is noted that in this study the CPIF index is only considered as a mathematical index, and it does not implicitly have any additional physical or mechanical meanings.

Based on the experimental data in Table 3 and Equation (11), sixteen average CPIFs were calculated and listed in Table 4.

Figure 5 shows the variation laws of CPIF with confining pressure. The CPIF continues to increase when the confining pressure rises, while discrepancies exist in the increment rates. This index grows steadily under low-axial static stresses (25, 50 and 75 MPa), while rapidly under the increased axial static stress (100 MPa). Such discrepancies can be demonstrated as follows: when the axial static stress is low enough and less than the elastic limits of rocks under each proposed confining pressure, the steady increment of CPIF is caused by the positive effect of the two types of static stresses on the strength enhancement. Conversely, when the axial static stress becomes higher (100 MPa) and exceeds the elastic limits of rocks corresponding to the low-confining pressure (0 and 5 MPa), but when it is still less than the elastic limits corresponding to the increased confining pressures (10 and 15 MPa), the axial static stress first weakens the rock and then strengthens the rock. In this situation, the effects of the two types of static stresses on the strength enhancement are opposite at first, and then become consistent to each other. Such a

Table 4. Average CPIFs.

Axial static stress (MPa)	Confining pressure (MPa)			
	0	5	10	15
25	1.00	1.16	1.36	1.55
50	1.00	1.16	1.33	1.49
75	1.00	1.17	1.35	1.51
100	1.00	1.34	1.72	2.05
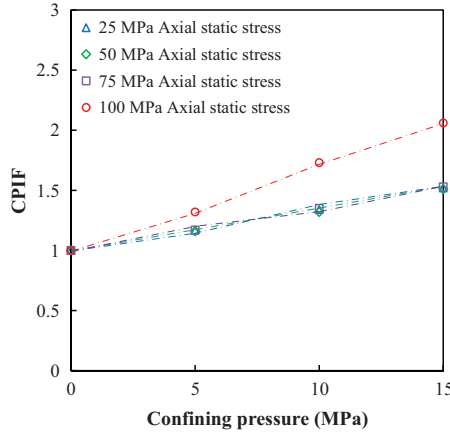
Figure 5. Variation laws of CPIF with confining pressure.

transformation can lead to a wider gap between the two consecutive values of CPIFs and yields a rapid increment as a result. Such a phenomenon, whereby the confining pressure strengthens the rock in a more significant way also takes place when the axial static stress reaches a particular level, which is equivalent to the rock's elastic limit.

3.3. Dynamic deformation behaviours

A cogent analysis on the dynamic deformation behaviours of rock should be based on an accurate definition of the deformation modulus. Nevertheless, such a modulus definition cannot indiscriminately copy the conventional one used for the elastic modulus in the static tests because it is difficult to identify a segment with a constant slope before the occurrence of the peaks of the stress–strain curves (Chen, Li, & Zhang, 2016), as shown in Figure 3. Thus, a modified definition is proposed with Equations (12) to (15), as schematic represented in Figure 6.

$$E_1 = \frac{\sigma_{50\%}}{\varepsilon_{50\%}} \tag{12}$$

$$E_2 = \frac{\sigma_p - \sigma_{50\%}}{\varepsilon_p - \varepsilon_{50\%}} \tag{13}$$

$$E_3 = \tan \alpha \tag{14}$$

$$E = \frac{1}{4}(E_1 + 2E_2 + E_3) \tag{15}$$

where, E is the dynamic deformation modulus; σ_p and $\sigma_{50\%}$ are the peak stress and 50% of peak stress, respectively; ε_p and $\varepsilon_{50\%}$ are the strains corresponding to the peak stress and 50% of peak stress individually; α is the angle between tangent at the 50% of peak stress and axis of strain. Besides, E_1, E_2 and E_3 were used to represent the partial slopes of the pre-peak curve, while their physical significances were not considered.
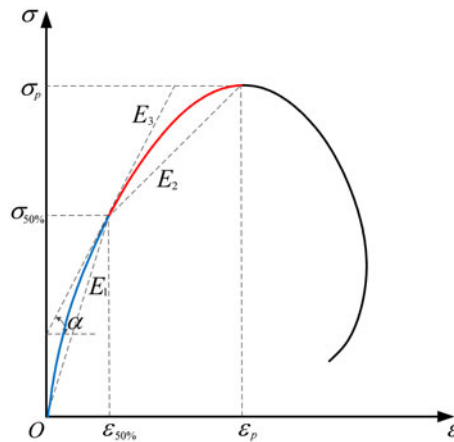
Figure 6. Schematic diagram of the modified dynamic deformation modulus.

Table 5. Calculated deformation moduli of rocks.

No.	Axial static stress (MPa)	Confining pressure (MPa)	Calculated deformation modulus (GPa)		
			Test 1	Test 2	Test 3
1	25	0	37.49	41.14	44.23
2	50	0	41.32	44.62	46.43
3	75	0	45.60	48.18	49.98
4	100	0	39.86	37.63	35.96
5	25	5	42.44	44.98	45.11
6	50	5	55.12	50.51	51.93
7	75	5	56.68	59.61	58.37
8	100	5	48.50	49.76	53.20
9	25	10	52.17	57.51	55.31
10	50	10	61.65	62.31	64.32
11	75	10	64.21	68.64	66.76
12	100	10	69.65	66.32	68.53
13	25	15	61.42	65.52	67.11
14	50	15	71.32	70.82	68.52
15	75	15	72.32	76.51	75.63
16	100	15	77.93	76.71	78.25

According to the modified definition, the dynamic deformation moduli of rocks were calculated and written in Table 5.

Figure 7 shows that the calculated deformation modulus changes with the axial static stress or confining pressure. Specifically, it grows as a function of the static stresses (including the axial static stress and confining pressure) when the rock remains in the linear elasticity under these static stresses, while it declined when the rock has suffered from damage before the impact. It is found that the dynamic deformation modulus yields a positive correlation with the compactness of the rock, and the compactness yields a negative relationship with the development of micro-cracks. Therefore, the variations in Figure 7 can be explained as follows: when the rock remains in the elastic stage under the static loading, the static stresses suppress the micro-crack propagation and augment the compactness, thus leading to an increase in the dynamic deformation modulus under the coupled loading. Conversely, when the rock enters the damage stage before the impact, the micro-cracks are re-activated and the rock compactness drops, thus the modulus decreases during the impact. Moreover, as shown in Figure 7(b), under increased axial static stresses, the confining pressure would play a more positive role in crack closures (as illustrated in Section 3.2), and thus result in an accelerating modulus growth. It is observed that the
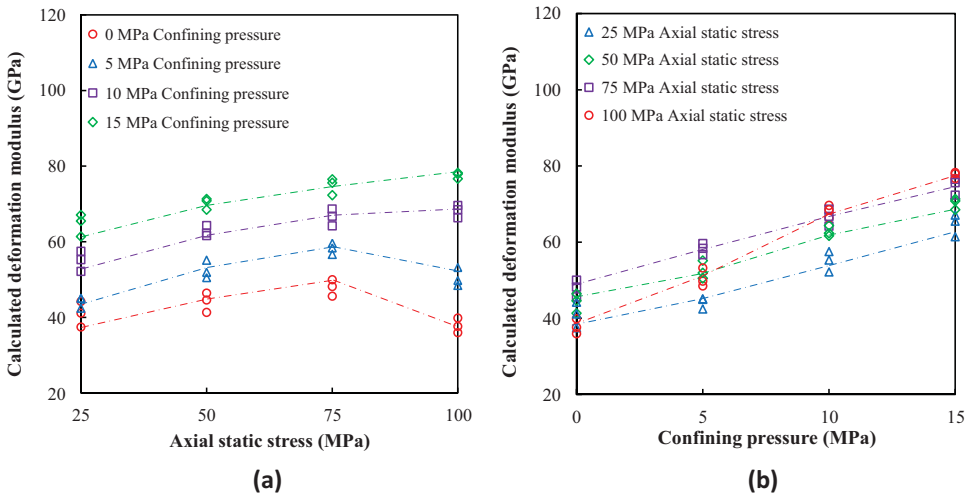
Figure 7. Variation laws of calculated deformation modulus (a) with axial static stress; (b) with confining pressure.
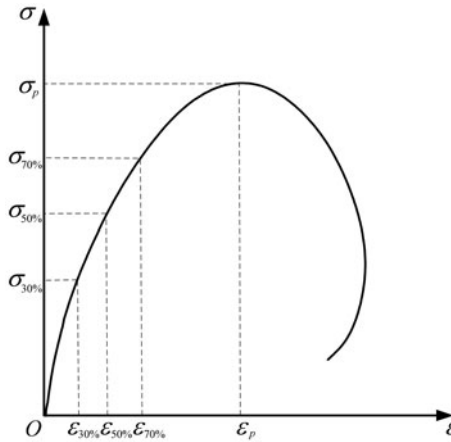

Figure 8. Parameters used in the three existing deformation modulus definitions.

variation laws can be theoretically explained in detail, and the modified definition can become available.

Furthermore, three existing modulus definitions were taken as comparisons; their relevant parameters are represented in Figure 8. And the corresponding deformation moduli of the rocks were calculated and averaged, as listed in Table 6.

From Figure 9(a), we can see that the deformation moduli derived based on definition (1) are not sensitive to an increasing axial static stress, and there are rarely obvious increments or reductions. Correspondingly, the moduli determined based on definition (2) begin to increase with the rising axial static stress when the rock is in the elastic stage while decrease when the rock enters the damage stage before the impact, but there are often some abnormal values that deviate from the overall trend. In addition, the variation laws for the moduli calculated based on definition (3) generally conform to the theoretical predictions. However, their values are not reasonable, and they are far smaller compared with the actual ones. In Figure 9(b), we can observe that although all the moduli increase with the confining pressure, none of them can characterise the differences in the growth rate under the different levels of axial static stresses.

Table 6. Average deformation moduli of rocks derived based on the three existing definitions (GPa).

| Definitions	Source	Axial static stress (MPa)	Confining pressure (MPa)			
			0	5	10	15
Definition (1) $E_{(1)} = \frac{\sigma_{50\%}}{\varepsilon_{50\%}}$	Fairhurst and Hudson (1999)	25	52.23	63.89	74.30	87.56
		50	54.56	64.87	77.12	89.63
		75	54.98	66.30	76.54	88.42
		100	53.68	66.03	75.12	89.31
Definition (2) $E_{(2)} = \frac{\sigma_{70\%} - \sigma_{30\%}}{\varepsilon_{70\%} - \varepsilon_{30\%}}$	Zhou, Zhang, Yang, and Wang (2015)	25	38.63	45.86	56.85	64.45
		50	35.21	50.63	60.52	71.86
		75	42.34	49.86	63.65	70.63
		100	41.42	47.71	60.02	66.34
Definition (3) $E_{(3)} = \frac{\sigma_p - \sigma_{50\%}}{\varepsilon_p - \varepsilon_{50\%}}$	(Gong, Li, and Liu (2011))	25	20.52	31.62	39.41	48.56
		50	28.42	35.36	46.87	55.41
		75	36.16	44.02	47.89	57.63
		100	20.00	34.34	45.62	51.98
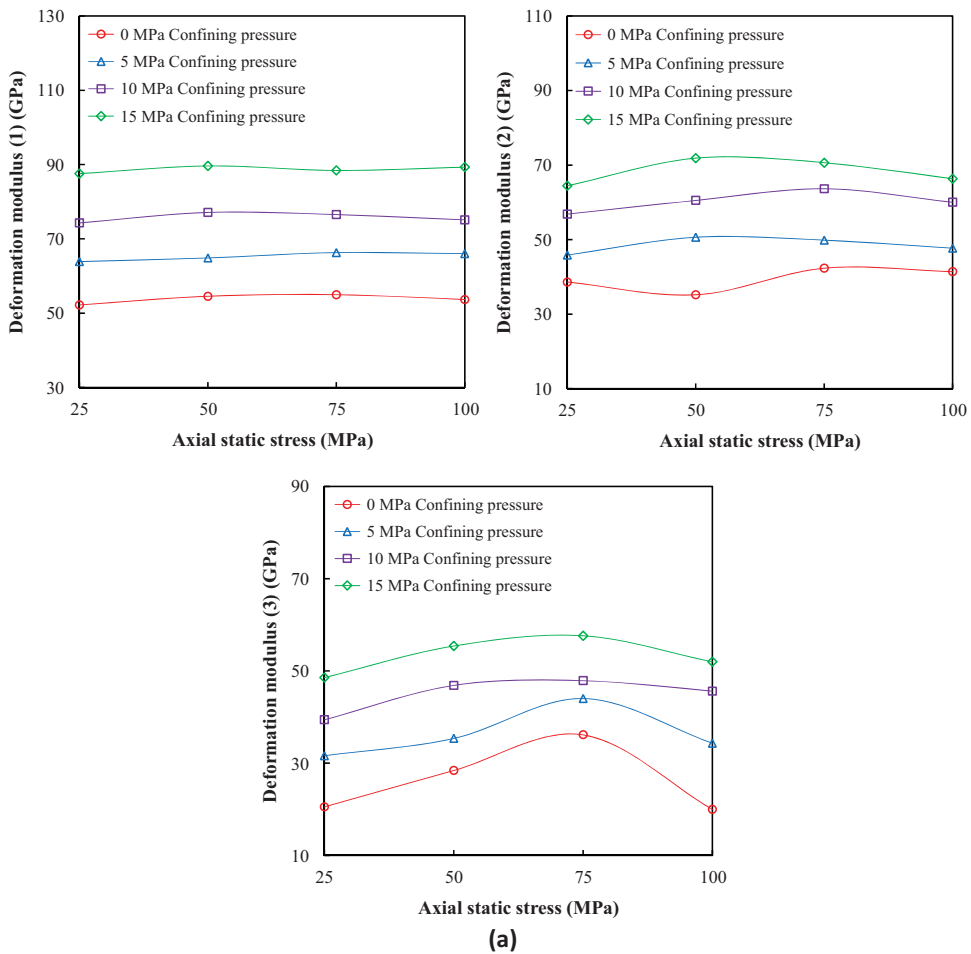
Figure 9. Variation laws of deformation moduli derived based on the three existing definitions (a) with axial static stress; (b) with confining pressure.

To summarise, none of the three deformation moduli exhibit good correspondence with the theoretically predicted trends, and each of these modulus types have their own deficiencies. By comparison, the modified definition proposed in this study is a better one, and can determine the dynamic deformation modulus with smaller errors and in more details.
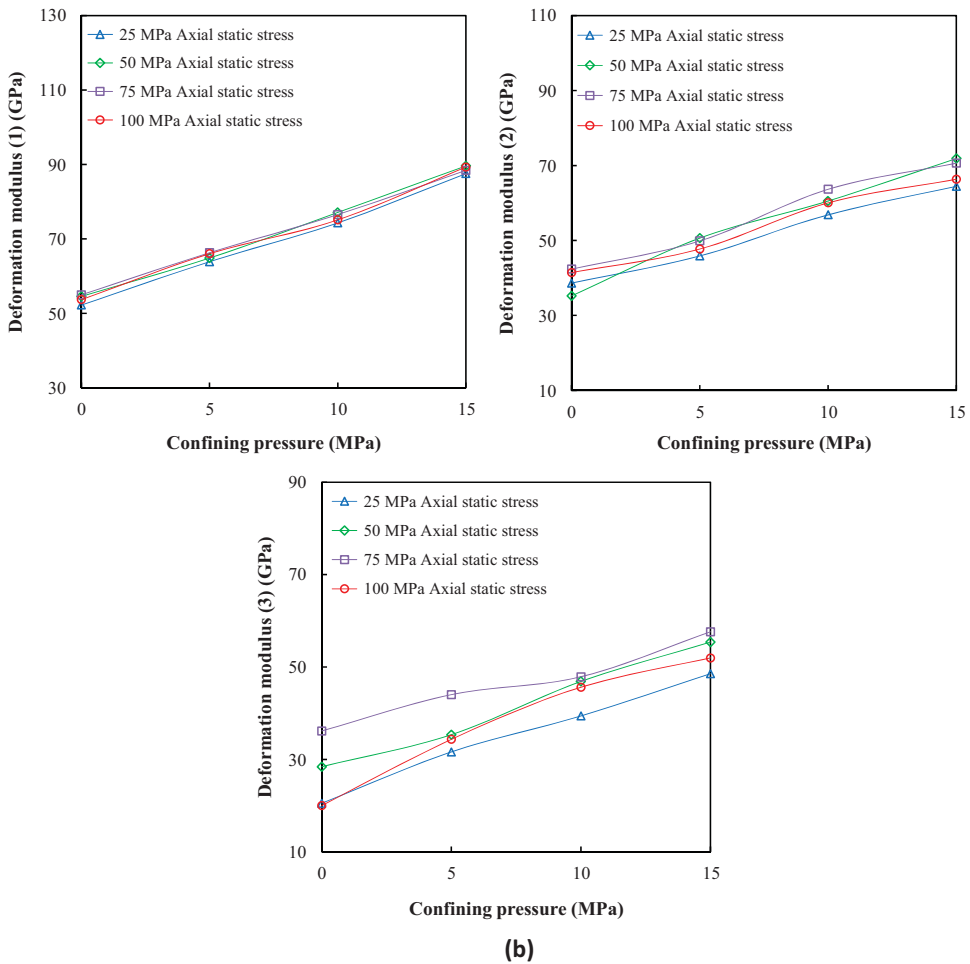
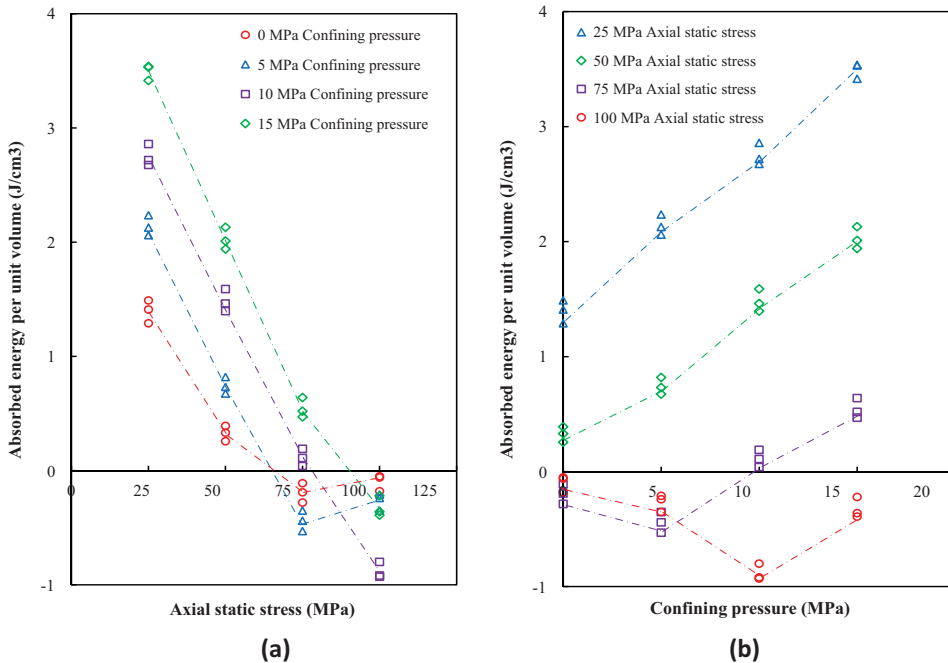Figure 9. Continued.

3.4. Energy absorption and release laws

The absorbed energy per unit volume is vital when studying the energy absorption and release laws of rocks during the impact (Rossmanith, 2014). They were calculated with Equations (7)–(10) and are listed in Table 7.

Figure 10 shows the variation laws of absorbed energy per unit volume with axial static stress or confining pressure. As shown in Figure 10(a), the absorbed energy per unit volume decreases from positive to negative values followed by a possible rebound toward values around zero under low-confining pressures. In Figure 10(b), the absorbed energy per unit volume grows overall, and the possibility of a temporary decrease is not ruled out under the increased axial static stresses.

There exists a complicated transformation mechanism in the energy absorption and release process. In particular, as the rock is subjected to the static stresses, it can deform and simultaneously store some initial energy within it. The initial energy increases with the rising static stresses and the growing deformation modulus when the rock stays in the elastic stage. Since the rock enters the early damage stage owing to the higher axial static stress, the initial energy continues to accumulate, then reaches the maximum value, and attains the so-called energy storage limit (ESL). At the time when the rock turns into the late damage stage, the initial energy

Table 7. Absorbed energy per unit volume of rocks.

No	Axial static stress (MPa)	Confining pressure (MPa)	Absorbed energy per unit volume (J/cm³)		
			Test 1	Test 2	Test 3
1	25	0	1.29	1.49	1.41
2	50	0	0.26	0.33	0.39
3	75	0	−0.11	−0.28	−0.19
4	100	0	−0.18	−0.06	−0.05
5	25	5	2.13	2.24	2.06
6	50	5	0.68	0.73	0.82
7	75	5	−0.44	−0.35	−0.53
8	100	5	−0.21	−0.35	−0.24
9	25	10	2.68	2.86	2.72
10	50	10	1.40	1.46	1.59
11	75	10	0.19	0.04	0.11
12	100	10	−0.93	−0.80	−0.92
13	25	15	3.42	3.54	3.53
14	50	15	2.13	1.94	2.01
15	75	15	0.64	0.47	0.52
16	100	15	−0.22	−0.39	−0.36

Figure 10. Variation laws of absorbed energy per unit volume (a) with axial static stress (b) with confining pressure.

continues to exist at the ESL. However, in this situation, the ESL itself is no longer constant, and it declines as a function of the growing axial static stress, or as a function of a decreasing confining pressure, thus the initial energy decreases subsequently and part of them are used for the micro-crack propagation. Herein, the ESL is considered as the maximum energy storage capacity of the rock, and it is positively correlated with the confining pressure. Additionally, the initial energy is treated as the energy storage value of the rock that is subjected to the static stresses before an impact and it has positive correlations with the transient axial static stress and the confining pressure.

When a dynamic loading that is sufficiently strong to smash the rock is applied, the ESL would play critical roles in the process of energy absorption and release in different situations. Specifically, when the initial energy is far from reaching the ESL, the rock can continue to deform and absorb the additional energy during the impact, and its absorption capacity is the difference between the initial energy and the ESL. When the rock has entered the early damage stage before the impact (Wang, Xu, Liu, Wang, & Liu, 2016), and as the initial energy becomes closer to, or attains the ESL, the rock has less or even no capacity to further absorb the energy. Conversely, it might release much of the initial energy owing to the slight disturbance. In this situation, the larger the ratio of the initial energy to the ESL is, the more energy the rock releases. Furthermore, when the rock has turned into the late damage stage under the static stresses, the energy release value is always proportional to the ESL during the impact.

Based on Figure 10(a), the variation laws under the different levels of confining pressures are approximately the same, and the case of a confining pressure of 5 MPa is used as an example. In the energy absorption domain of 0–64 MPa ($\sim$50% of static peak stress), the decrease (from an average of 2.14–0.74 J/cm^3, and then to zero) is caused by the narrower gap between the increasing initial energy and the ESL. Additionally, at $\sim$64 MPa, the absorbed energy per unit volume reaches zero, and there exists an equilibrium between the energy absorption and release. Then, in the energy release domain of 64–75 MPa, the downward trend (from zero to an average of -0.44 J/cm^3) is attributed to the increasing ratio of the growing initial energy to the ESL. Furthermore, at 75 MPa, the absorbed energy per unit volume approaches the lowest value (average of -0.44 J/cm^3) and the rock releases the maximum energy, which is attributed to the existence of the initial energy that reaches the ESL. Moreover, in the energy release domain of 75–100 MPa, the rebound phenomenon (from an average of -0.44 up to -0.26 J/cm^3) is owing to the descending initial energy accompanying the declining ESL.

In Figure 10(b), the growth in the energy absorption domain is owing to the wider gap between the initial energy and the increased ESL. Conversely, in the energy release domain, the downward trend is caused by the increasing initial energy accompanying the increased ESL. The upward trend, however, results from the decreasing ratio of the initial energy to the increased ESL.

4. Conclusions

The effects of the axial static stress and confining pressure on the dynamic compressive behaviours of granite under the 3D coupled static–dynamic loading were investigated using a modified SHPB system. Simultaneously, a new index of confining pressure increase factor (CPIF) was introduced, a modified definition of dynamic deformation modulus was derived, and the roles of the energy storage limit (ESL) were highlighted. The main conclusions are as follows:

1. The axial static stress tends to either strengthen or weaken the rocks in different situations. Specifically, there exists a particular threshold value that is equivalent to the rock's elastic limit. The axial static stress has a positive effect on the strength enhancement when it is less than the threshold value, otherwise, it has a negative effect

2. The confining pressure contributes to the strength enhancement of the rocks under the coupled loading and strengthens the rocks in a more significant way at the time when the axial static stress reaches a particular level that is equivalent to the rock's elastic limit, thereby eliciting a stronger CPIF sensitivity to the confining pressure

3. The dynamic deformation modulus increases as a function of the static stresses (including the axial static stress and confining pressure) when the rock remains in the linear elasticity under the static loading, and it declines when the rock has suffered from damage before the impact. Furthermore, the modified definition can adequately characterise the pre-peak

stress–strain curves and determine the deformation modulus with less error and in more details

4. The ESL tends to play critical roles in the process of energy absorption and release in different situations during the impact: the difference between the ESL and the initial energy determines the energy absorption value. The ratio between them derives the energy release value when the rock has entered the early damage stage under the static stresses. The ESL itself is proportional to the energy release value when the rock has gone into the late damage stage before it is subjected to dynamic loading

Disclosure statement

No potential conflict of interest was reported by the authors.

References

ASTM. (2001). *Standard test method for compressive strength of cylindrical concrete specimens*. West Conshohocken: ASTM International.

Chen, Z. M., Li, Y. X., & Zhang, Z. (2016). Experimental study of dynamic mechanical properties of granite. *Applied Mechanics and Materials*, *858*, 86–90.

Dai, F., Huang, S., Xia, K. W., & Tan, Z. Y. (2010). Some fundamental issues in dynamic compression and tension tests of rocks using split hopkinson pressure bar. *Rock Mechanics and Rock Engineering*, *43*(6), 657–666.

Du, H. B., Dai, F., Xu, Y., Liu, Y., & Xu, H. N. (2018). Numerical investigation on the dynamic strength and failure behaviour of rocks under hydrostatic confinement in SHPB testing. *International Journal of Rock Mechanics and Mining Sciences*, *108*, 43–57.

Fairhurst, C. E., & Hudson, J. A. (1999). Draft ISRM suggested method for the complete stress-strain curve for intact rock in uniaxial compression. *International Journal of Rock Mechanics and Mining Sciences*, *36*(3), 279–289.

Feng, J., Wang, E., Shen, R., Chen, L., Li, X., & Xu, Z. (2016). Investigation on energy dissipation and its mechanism of coal under dynamic loads. *Geomechanics and Engineering*, *11*(5), 657–670.

Gong, F. Q., Li, X. B., & Liu, X. L. (2011). Preliminary experimental study of characteristics of rock subjected to 3D coupled static and dynamic loads. *Chinese Journal of Rock Mechanics and Engineering*, *30*(6), 1179–1190.

Hashiba, K., & Fukui, K. (2015). Index of loading-rate dependency of rock strength. *Rock Mechanics and Rock Engineering*, *48*(2), 859.

Jiang, Q., Zhong, S., Cui, J., Feng, X. T., & Song, L. B. (2016). Statistical characterization of the mechanical parameters of intact rock under triaxial compression: an experimental proof of the Jinping Marble. *Rock Mechanics and Rock Engineering*, *49*(12), 4631–4646.

Latham, J. P., Van Meulen, J. A., & Dupray, S. (2006). Prediction of fragmentation and yield curves with reference to armourstone production. *Engineering Geology*, *87*(1-2), 60–74.

Li, J. J., Hu, M. S., Ding, E. J., Kong, W., Pan, D. M., & Chen, S. E. (2016). Multi-parameter numerical simulation of dynamic monitoring of rock deformation in deep mining. *International Journal of Mining Science and Technology*, *26*(5), 851–855.

Li, X. B., Tao, M., Wu, C. Q., Du, K., & Wu, Q. H. (2017). Spalling strength of rock under different static pre-confining pressures. *International Journal of Impact Engineering*, *99*, 69–74.

Li, X. B., Zhou, Z. L., Zhao, F. J., Zuo, Y. J., Ma, C. D., Ye, Z. Y., & Hong, L. (2009). Mechanical properties of rock under coupled static-dynamic loads. *Journal of Rock Mechanics and Geotechnical Engineering*, *1*(1), 41–47.

Li, X. B., Lok, T. S., & Zhao, J. (2005). Dynamic characteristics of granite subjected to intermediate loading rate. *Rock Mechanics and Rock Engineering*, *38*(1), 21–39.

Li, X. B., Lok, T. S., Zhao, J., & Zhao, P. J. (2000). Oscillation elimination in the Hopkinson bar apparatus and resultant complete dynamic stress-strain curves for rocks. *International Journal of Rock Mechanics and Mining Sciences*, *37*(7), 1055–1060.

Liang, C. Y., Zhang, Q. B., Li, X., & Xin, P. (2016). The effect of specimen shape and strain rate on uniaxial compressive behaviour of rock material. *Bulletin of Engineering Geology and the Environment*, *75*(4), 1669–1681.

Liu, N., Li, M., & Chen, W. M. (2017). Mechanical deterioration of rock salt at different confinement levels: A grain-based lattice scheme assessment. *Computers and Geotechnics*, *84*, 210–224.

Liu, E. L., & He, S. M. (2012). Effects of cyclic dynamic loading on the mechanical properties of intact rock samples under confining pressure conditions. *Engineering Geology*, *125*, 81–91.

Mishra, S., Meena, H., Chakraborty, T., Chandel, P., & Singh, M. (2017). High strain rate characterization of Himalayan dolomite. *Procedia Engineering*, *173*, 822–829.

Mohr, D., Gary, G., & Lundberg, B. (2010). Evaluation of stress-strain curve estimates in dynamic experiments. *International Journal of Impact Engineering*, *37*(2), 161–169.

Munoz, H., Taheri, A., & Chanda, E. K. (2016). Pre-peak and post-peak rock strain characteristics during uniaxial compression by 3D digital image correlation. *Rock Mechanics and Rock Engineering*, *49*(7), 2541–2554.

Niu, Y., Li, K. G., Liu, D. K., Li, X. L., & Peng, S. J. (2015). Experimental investigation on shock mechanical properties of red sandstone under preloaded 3D static stresses. *Journal of Engineering Science and Technology Review*, *8*(5), 205–211.

Rossmanith, H. P. (2014). *Rock fracture mechanics*. New York, NY: Springer.

Saksala, T., Hokka, M., & Kuokkala, V. T. (2017). Numerical 3D modeling of the effects of strain rate and confining pressure on the compressive behaviour of Kuru granite. *Computers and Geotechnics*, *88*, 1–8.

Saksala, T. (2016). Numerical study of the influence of hydrostatic and confining pressure on percussive drilling of hard rock. *Computers and Geotechnics*, *76*, 120–128.

Sun, Y. K., Li, Q., Yang, D. X., Fan, C. K., & Sun, A. (2016). Investigation of the dynamic strain responses of sandstone using multichannel fiber-optic sensor arrays. *Engineering Geology*, *213*, 1–10.

Tian, H. M., Chen, W. Z., Yang, D. S., & Yang, J. P. (2015). Experimental and numerical analysis of the shear behaviour of cemented concrete-rock joints. *Rock Mechanics and Rock Engineering*, *48*(1), 213–222.

Wang, Z. L., & Shi, G. Y. (2017). Effect of heat treatment on dynamic tensile strength and damage behaviour of medium-fine-grained Huashan granite. *Experimental Techniques*, *41*, 1–11.

Wang, P., Xu, J. Y., Fang, X. Y., & Wang, P. X. (2017). Energy dissipation and damage evolution analyses for the dynamic compression failure process of red-sandstone after freeze-thaw cycles. *Engineering Geology*, *221*, 104–113.

Wang, P., Xu, J. Y., Liu, S., Wang, H. Y., & Liu, S. H. (2016). Static and dynamic mechanical properties of sedimentary rock after freeze-thaw or thermal shock weathering. *Engineering Geology*, *210*, 148–157.

Wang, Q. Z., Li, W., & Song, X. L. (2006). A method for testing dynamic tensile strength and elastic modulus of rock materials using SHPB. *Pure and Applied Geophysics*, *163*(5-6), 1091–1100.

Wu, B. B., Chen, R., & Xia, K. W. (2015). Dynamic tensile failure of rocks under static pre-tension. *International Journal of Rock Mechanics and Mining Sciences*, *80*, 12–18.

Xia, K. W., & Yao, W. (2015). Dynamic rock tests using split Hopkinson (Kolsky) bar system—A review. *Journal of Rock Mechanics and Geotechnical Engineering*, *7*(1), 27–59.

Zhang, P., Mishra, B., & Heasley, K. A. (2015). Experimental investigation on the influence of high pressure and high temperature on the mechanical properties of deep reservoir rocks. *Rock Mechanics and Rock Engineering*, *48*(6), 2197–2211.

Zhang, Q. B., & Zhao, J. (2014). A review of dynamic experimental techniques and mechanical behaviour of rock materials. *Rock Mechanics and Rock Engineering*, *47*(4), 1411–1478.

Zhao, Y. X., Liu, S. M., Jiang, Y. D., Wang, K., & Huang, Y. Q. (2016). Dynamic tensile strength of coal under dry and saturated conditions. *Rock Mechanics and Rock Engineering*, *49*(5), 1709–1720.

Zhao, J., & Li, H. B. (2000). Experimental determination of dynamic tensile properties of a granite. *International Journal of Rock Mechanics and Mining Sciences*, *37*(5), 861–866.

Zhou, Z. H., Zhang, Y. Q., Yang, G. A., & Wang, C. (2015). Experimental study on mechanical characteristics of dolomite under three-dimensional coupled static-dynamic loading. *Journal of China Coal Society*, *40*(05), 1030–1036.

Zhou, Z. L., Li, X. B., Zou, Y., Jiang, Y. H., & Li, G. N. (2014). Dynamic Brazilian tests of granite under coupled static and dynamic loads. *Rock Mechanics and Rock Engineering*, *47*(2), 495–505.

Zhou, Y. X., Xia, K., Li, X. B., Li, H. B., Ma, G. W., Zhao, J., … Dai, F. (2012). Suggested methods for determining the dynamic strength parameters and mode-I fracture toughness of rock materials. *International Journal of Rock Mechanics and Mining Sciences*, *49*, 105–112.